RSC Advances

ROYAL SOCIETY OF CHEMISTRY

www.rsc.org/advances

RSC Advances

ARTICLE

Fabrication and enhanced the simulated sunlight photocatalytic activity of metallic platinum and indium oxide codoped titania nanotubes

Received 00th January 20xx,
Accepted 00th January 20xx

DOI: 10.1039/x0xx00000x

www.rsc.org/

Fengyan Ma,[a,*] Zhi Geng[b] and Jiyan Leng[c]

Metallic platinum and indium oxide codoped titania nanotubes were fabricated by multicomponent assembly combined with solvothermal treatment. The structure, morphology, and optical properties of the prepared samples were comparatively characterized. The Pt/In_2O_3–TiO_2 nanotubes exhibited anatase phase with homogeneously dispersed metallic Pt nanoparticles on the surface. Under the simulated sunlight irradiation, the photocatalytic performance of the samples was tested in degradation of dye rhodamine B (RB) and diethyl phthalate (DEP). Compared to In_2O_3–TiO_2 and TiO_2 nanotubes as well as Pt/In_2O_3–TiO_2 nanoparticles, Pt/In_2O_3–TiO_2 nanotubes with 0.8% Pt and 9.4% In_2O_3 doping exhibited higher photocatlytic activity, and nearly total degradation of dye RB (20 mg L^{-1}) or DEP (10 mg L^{-1}) was obtained after 50 or 45 min under simulated light irradiation. Reasons for the enhanced photocatalytic activity were revealed.

Keywords: Platinum; Indium oxide; Titania; Nanotubes; Photocatalysis

1. Introduction

Recently, one-dimensional (1D) TiO_2 nanomaterials have attracted great attention because of their interesting properties and widespread applications in the photovoltaic, photocatalytic, electrochemical, and gas sensing fields[1, 2]. Among various 1D TiO_2 nanomaterials, TiO_2 nanotube is currently one of the most promising photocatlyst. In comparison to TiO_2 nanoparticles, the open mesoporous morphology of TiO_2 nanotubes have many useful features as follow[3-5]: (i) channelled structure can efficiently transfer electrons along the 1D parth; (ii) high surface area enables it to adsorb a large amount of chemicals; (iii) the unique structure makes better use of light through multiple reflections within its hollow space. Therefore, TiO_2 nanotubes can be served not only as the photocatalysts but also as good substrates for the enhancement of photocatalytic activity by modification. Although TiO_2 possessed such promising potentials, its relatively poor charge transport property and wide bandgap (~3.2 eV) are two main limitations for its contemporary applications in catalysis and energy harvesting/storage.

However, the overall quantum efficiency of pure TiO_2 is relatively low. A key issue in developing new types of function TiO_2 materials is how to improve their photocatalytic efficiency. Herein a metallic platinum particles and indium oxide comodified titania nanotube system (Pt/In_2O_3–TiO_2-NT) was demonstrated. On the one hand, In_2O_3 is a low band gap (2.8 eV) semiconductor, the incorporation of In_2O_3 is expected to extend the light response of TiO_2 to a higher wavelength region and thereby decreasing its band gap[6]; meanwhile, TiO_2 coupled with In_2O_3 may promote the efficient separation of the h_{VB}^{+}–e_{CB}^{-} pairs and therefore increasing the quantum yield[7]. On the other hand, deposition of metallic platinum particles throughout TiO_2 nanotubes is based on their surface plasmon effects, which can lead to field enhancement in the vicinity of Pt particles and thus allowing more efficient charge transfer by capturing the e_{CB}^{-}[8].

So far three main routes have been developed to make TiO_2 nanotubes, i.e. via templating, anodic oxidation, and hydrothermal synthesis methods[9, 10]. The extensive applications of the templating method may be limited due to the cost, insufficient characterization of template, and a concern over long-term instability of TNT products. The anodic oxidation method is time-consuming and special conditions are needed. Furthermore, this preparation process suffers from an environmental concern, as the anodization of Ti foil must be processed in highly toxic hydrofluoric acid aqueous solutions. The sizes or diameters of the TiO_2 nanomaterials obtained from the template and electrochemical anodization methods are often large, which lead to the low BET surface areas and disadvantages for the photocatalytic reactions[11, 12]. However, hydrothermal synthesis method has

[a] College of Chemistry and Chemical Engineering, Qiqihar University, Qiqihar 161006, Heilongjiang, PR China
[b] School of Environment, Northeast Normal University, Changchun 130117, PR China.
[c] First hospital of Jilin University, Jilin University, Changchun 130021, PR China
† Corresponding authors.
Tel.: +86 452 2742575. E-mail address: mafengyan989@163.com
Electronic Supplementary Information (ESI) available: Textural parameters, TEM, HRTEM images, FT-IR spectra, and TOC of samples datas. See DOI: 10.1039/x0xx00000x

been adapted to produce high yields of TNTs with vast pore and unique nanotubular structures. As for incorporation of the components within TiO_2 nanotubes, ion-exchange or impregnation method is generally applied[13]. The process suffers from problems such as leaching, aggregation and poor control over the loadings of the doped component. In the case of noble metal doping, the generally used photodeposition and chemical reduction methods have the disadvantages of hard control of the size of the metal and severe aggregation of the metal clusters[14-16]. Therefore, the new requirements on the preparation route are put forward.

In the present work, Pt/In_2O_3–TiO_2 nanotubes (Pt/In_2O_3–TiO_2-NT) were fabricated by multicomponent assembly approach combined with solvothermal treatment using titanic acid nanotubes as the staring materials in the absence of any reducing agents or stabilizing ligands. Subsequently, their simulated sunlight photocatalytic activity was evaluated by the degradation of dye Rhodamine B (RB) and a kind of light insensitive compound, diethyl phthalate (DEP). Furthermore, the photoelectrochemical experiment indicated that the separation efficiency of the photo-generated electron–hole pairs was largely improved, and this led to a much higher photocatalytic activity for organic pollutant degradation. The relationship between the morphology, structure, optical properties and the photocatalytic activities of Pt/In_2O_3–TiO_2-NTs was investigated in detail.

2. Experimental

2.1. Catalyst preparation

2.1.1. Titanic acid nanotubes

Titanium tetraisopropoxide (TTIP, 3.0 mL) was dissolved in isopropanol (*i*-PrOH, 18 mL) under vigorous stirring at room temperature for 0.5 h. Water (0.9 mL) was then added dropwise into the TTIP/*i*-PrOH solution under vigorously stirring for 6 h. The mixture was dried at 353 K for 12 h followed by calcination at 773 K for 3 h. The resulting TiO_2 powder (0.5 g) was dispersed into NaOH solution (10 mol L^{-1}, 25 mL), and the suspension was ultrasonicated for 30 min followed by hydrothermal treatment at 423 K for 48 h (heating rate of 2 K min^{-1}). The obtained precipitate was washed with HCl (0.1 mol L^{-1}) and water to pH 6–7, and then it was dried at 353 K overnight. In this case, titanic acid nanotubes were successfully prepared.

2.1.2. Pt/In_2O_3–TiO_2 nanotubes

The as-prepared titanic acid nanotubes (0.46 g) were dispersed into ethanol (EtOH, 16 mL) under vigorous stirring at room temperature. Subsequently, $InCl_3{\cdot}4H_2O$ (0.14 g and 0.31 g)/H_2O (0.66 mL)/EtOH (2 mL) and $H_2PtCl_6{\cdot}6H_2O$ (0.01 g, 0.03 g, and 0.12 g)/EtOH (2 mL) solutions were added dropwise into the above suspension successively under vigorously stirring. The resulting mixture was suffered from solvolthermal treatment at 423 K for 6 h (heating rate of 2 K min^{-1}), and the resulting precipitate was dried and washed with deionized water. The obtained powder was further dried at 353 K overnight prior to annealing in nitrogen gas flow at 673 K for 0.5 h. The final product was denoted as Pt/In_2O_3–TiO_2–NTs-(x, y), where x and y represent the doping of Pt and In_2O_3 (wt%), respectively. For comparison, the Pt/In_2O_3–TiO_2–NTs-(x, y)-573 K and Pt/In_2O_3–TiO_2–NTs-(x, y)-773 K materials were prepared under the calcination temperature at 573 K and 773 K in nitrogen gas flow, respectively.

2.1.3. Pt/In_2O_3–TiO_2 nanoparticles

TTIP (1.7 mL) was dissolved in *i*-PrOH (16 mL) under vigorous stirring at room temperature for 0.5 h, and then $InCl_3{\cdot}4H_2O$ (0.14 g)/H_2O (0.66 mL)/EtOH (2 mL) and $H_2PtCl_6{\cdot}6H_2O$ (0.03 g)/EtOH (2 mL) solutions were added dropwise into the above suspension successively under vigorously stirring. The subsequent steps are the same as those of the Pt/In_2O_3–TiO_2–NTs, and the product was denoted as Pt/In_2O_3–TiO_2–NPs-(x, y), where x and y represent the weight percentage or doping of Pt and In_2O_3 (wt %) in the products, respectively.

2.2. Preparation of Pt/In_2O_3–TiO_2–NTs/Ti electrode

The rectangle titanium (Ti) sheets (size 10 × 50 mm, thickness 140 μm, purity > 99.6%) were cleaned ultrasonically in water and alcohol for 10 min, respectively. The cleaned Ti sheets were chemically etched in a mixture of HF, HNO_3, and H_2O for 30 s (HF: HNO_3: H_2O = 1: 4: 5; v/v/v) followed by rinsing with distilled water and drying in argon flow at room temperature. The obtained Pt/In_2O_3–TiO_2–NTs were well dispersed in ethanol solution under vigorous stirring for 3 h at room temperature in an open beaker. The obtained suspension was used for spin-coating Ti sheet at an initial spin rate of 5000 rpm for 6 s and then 2000 rpm for 6 s. After aging at room temperature for 12 h, the sheet was washed three times with water, and then dried at 353 K overnight. For a comparison, TiO_2–NTs/Ti, In_2O_3–TiO_2–NTs/Ti, and Pt/In_2O_3–TiO_2–NPs/Ti photoanodes were also prepared by the same process.

2.3. Catalyst characterization

In_2O_3 and Pt loadings were determined by a Leeman Prodigy Spec ICP-AES. X-ray diffraction patterns were obtained on a D/max-2200 VPC diffractometer using Cu Kα radiation. XPS was performed on a VG-ADES 400 instrument with Mg Kα-ADES source at a residual gas pressure of below 10^{-8} Pa. Raman scattering spectra were recorded on a Jobin-Yvon HR 800 instrument with an Ar^+ laser source of 488 nm wavelength in a macroscopic configuration. Nitrogen porosimetry measurement was performed on a Micromeritics ASAP 2020M surface area and porosity analyzer after the samples were outgassed under vacuum at 363 K for 1 h and 423 K for 6 h. Field-emissing scanning electron microscope (FESEM) images were obtained on a XL-30 ESEM FEG field emission scanning electron microscope at 20 kV. Transmission electron microscope (TEM) and high resolution transmission electron microscope (HRTEM) were taken on a JEM-2100F at an accelerating voltage of 200 kV. UV–vis/DRS were recorded on a Cary 500 UV–vis–NIR spectrophotometer. Fourier transform infrared (FT-IR) spectra were recorded on a Nicolet Magna 560 IR spectrophotometer. Changes of total organic carbon (TOC) in DEP degradation systems were monitored by a Shimadzu TOC-500 Total Organic Carbon analysis system.

2.4. Photocatalytic tests

The simulated sunlight irradiation was supplied by a self-made solar simulator equipped with a 350 W xenon lamp and an IR cut filter. The equipment can provide uniform solar irradiance with the intensity from 0.1 W cm^{-2} (AM1.5G artificial sunlight, ASTM E927-05 Class A standard) to 0.3 W cm^{-2}; meanwhile, its spectrum matches

well with the natural solar light with main emission from 320 nm to 680 nm. The photocatalytic reaction was carried out in a self-made quartz photoreactor with a diameter of 63 mm. The suspension containing the solid catalyst (100 mg) and an aqueous solution of RB (20 mg L^{-1}, 100 mL) or DEP (10 mg L^{-1}, 100 mL) was ultrasonicated for 10 min and then stirred for 60 min in the dark. The reaction temperature was maintained at 303 ± 2 K by circulation of water through an external cooling jacket. Decreases of the concentrations of RB were analyzed by a Cary 500 UV–vis–NIR spectrophotometer at λ = 553 nm. Changes of DEP concentrations were monitored by a Shimadzu LC-20A HPLC: C_{18} column, UV detector (λ = 227 nm), acetonitrile/water (80/20 v/v), and 0.9 mL min^{-1}.

2.5. Photoelectrochemical experiment

Photocurrent measurement was carried out using the conventional three electrode setup connected to an electrochemical station (CH Instrument 660C, Shanghai Chenhua, China). In this electrochemical system, Pt/In_2O_3–TiO_2–NTs/Ti, In_2O_3–TiO_2–NTs/Ti, TiO_2–NTs/Ti or Pt/In_2O_3–TiO_2–NPs/Ti (effective area is 4 cm^2) was used as a working photoanode, and a Pt sheet (size 30 × 40 mm, purity 99.99%) and an Ag/AgCl (saturated KCl) electrode were used as the counter electrode and reference electrode, respectively. The electrolyte was 0.01 mol L^{-1} Na_2SO_4 aqueous solution (110 mL), and the distance between Ti sheet and Pt sheet was fixed at 30 mm. An external 125 W high-pressure mercury lamp was used as light source. The distance between Ti sheet and light source was fixed at 80 mm. The measurements were carried out at a constant potential of +1.0 V to the working photoanode.

3. Results and discussion

3.1. Catalyst characterization

3.1.1. Compositional and structural information

The crystalline phase of composite material was measured by XRD. As shown in Fig. 1a, the firstly prepared titanic acid nanotubes ($H_2Ti_2O_5{\cdot}H_2O$) exhibited orthorhombic phase with the characteristic diffractions at 9.2° (200), 24.2° (110), 28° (310), and 48° (020), respectively (JCPDS 47−0124)[17]. While with increasing In_2O_3 loading form 0 to 12%, In_2O_3–TiO_2–NTs were the mixture of anatase and rutile: the peaks at 25.3° (101), 37.8° (004), 48.1° (200), 53.9° (105), 55.1° (211), 62.7° (204), 68.8° (116), 70.3° (220), 75.3° (215), and 82.5° (224) corresponded to anatase phase structure (JCPDS 21–1272); and the peaks at 27.3° (110), 35.8° (101), and 40.9°(111) originated from rutile phase (JCPDS 01–76–0320). These results indicated the high In_2O_3 loading was beneficial to phase transformation form anatase into rutile. Additionally, the diffractions related to the In_2O_3 were not found, implying homogeneous dispersion of the In_2O_3 throughout the materials.

The crystalline phases of as-prepared composites with various Pt dopings (0 to 6.9%) were further studied (Fig. 1b). The major phase of all the tested samples was the anatase structure regardless of Pt loadings in the products. Up to 0.8 wt %, no diffractions corresponding to Pt were observed, which indicated that Pt was dispersed uniformly in the TiO_2–NT. The Pt/In_2O_3–TiO_2–NTs-(6.9, 12.0) showed peaks at 2Θ values of 39.8° and 46.3°, which are the characteristic peaks corresponding to the (111) and (200) planes of the facecentered cubic crystal of metallic platinum nanoparticles[18]. Fig. 1c showed the XRD patterns of the Pt/In_2O_3–TiO_2–NTs-(0.8, 9.4) composites obtained at different calcination temperatures. It is found that all the tested samples exhibited anatase phase. Moreover, these diffraction peaks became sharper as the calcination temperature was increased.

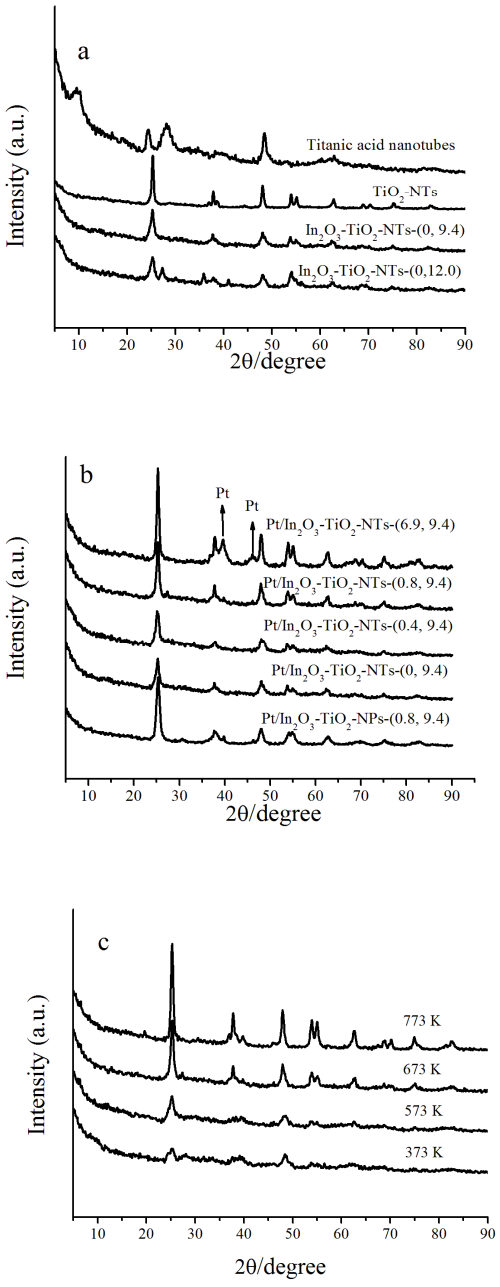

Fig. 1 XRD patterns of as-prepared (a) titanic acid nanotubes, and Pt/In_2O_3–TiO_2–NTs-(0, y) with y = 0, 9.4, and 12.0%, respectively; (b) Pt/In_2O_3–TiO_2–NTs-(x, 9.4) with x = 0, 0.4, 0.8, and 6.9%, respectively, and Pt/In_2O_3–TiO_2–NPs-(0.8, 9.4); (c) Pt/In_2O_3–TiO_2–NTs-(0.8, 9.4) calcined at different temperatures.

The surface chemical composition of the as-prepared TiO_2-based nanotubes was investigated by XPS technique. As shown in Fig. 2a, the determined binding energies of Ti $2p_{3/2}$ and Ti $2p_{1/2}$ were 458.1 eV and 463.8 eV, respectively, characteristic of the Ti (IV) oxidation state in the Ti–O bonds of bulk TiO_2 nanotubes. After introduction of the In_2O_3 or In_2O_3 and Pt into the TiO_2 nanotubes, the binding energies of Ti $2p_{3/2}$ and Ti $2p_{1/2}$ shifted to higher values. It indicates that a slight perturbation of titanium environment occurred due to In_2O_3 doping or In_2O_3 and Pt co-doping. The typical high-resolution XPS spectra of In 3d were displayed in Fig. 2b. The peaks at 444.6 eV and 452.2 eV (for Pt/In_2O_3–TiO_2–NTs-(0, 9.4)), and 444.9 eV and 452.2 eV (for Pt/In_2O_3–TiO_2–NTs-(6.9, 9.4)) were signed to In $3d_{5/2}$ and In $3d_{3/2}$, respectively, which were characteristic of In^{3+} in In_2O_3[6]. As to the high-resolution XPS spectrum of the Pt 4f, two peaks at 70.3 and 74.0 eV in Pt/In_2O_3–TiO_2–NTs-(6.9, 9.4) sample were signed to metallic platinum, indicating that the platinum species existing in the product was metallic Pt (Pt^0) rather than Pt^{2+} or Pt^{4+} ion[19, 20]. Thus, we can confirm that the In_2O_3 or In_2O_3 and Pt successfully doped in TiO_2–NTs.

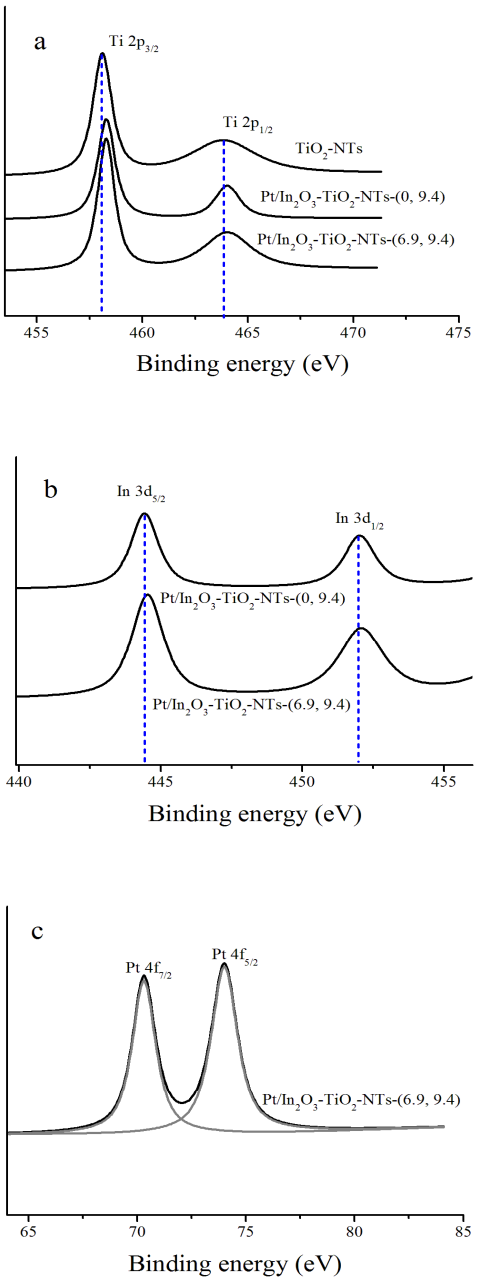

Fig. 2 XPS spectra of the TiO_2–NTs, Pt/In_2O_3–TiO_2–NTs-(0, 9.4), and Pt/In_2O_3–TiO_2–NTs-(6.9, 9.4) materials in the Ti 2p (a), In 3d (b), and Pt 4f (c) binding energy regions.

Fig. 3 showed the Raman spectra of TiO_2-based nanotubes. For comparison, TiO_2 nanoparticles (TiO_2–NPs) were tested under the same conditions. TiO_2–NPs were characterised by well-defined peaks at 144 cm^{-1} (E_g), 399 cm^{-1} (B_{1g}), 513 cm^{-1} (A_{1g}), and 639 cm^{-1} (E_g) which corresponded to the anatase structure[21]. As for the TiO_2–NTs, in addition to anatase peaks, the 280 cm^{-1} Raman peak of TiO_2–NTs appeared after forming the tubular structure and was associated with Ti–O–H bond resulting from proton exchange with HCl; The peak at 450 cm^{-1} was assigned to the Ti–O–Ti vibrations, whereas the bands at 700 cm^{-1} and 917 cm^{-1} were attributed to Ti–O–Na vibrations in the interlayer regions of the nanotube walls[22, 23]. As for the In_2O_3–TiO_2–NTs-(0, 9.4) and Pt/In_2O_3–TiO_2–NTs-(0.8, 9.4), the characteristic peak at 639 cm^{-1} (E_g) become intensively sharper; however, peaks at 280 cm^{-1} and 450 cm^{-1} became weaken, even peaks at 700 cm^{-1} and 917 cm^{-1} completely disappeared. These results revealed that the order degree of tubular structures of the composite reduced, but still maintained their tubular structures.

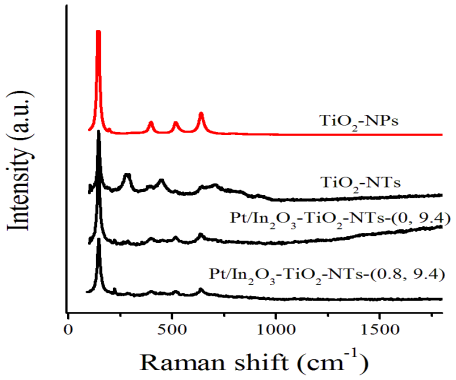

Fig. 3 Raman spectra of as-prepared TiO_2–NPs, TiO_2–NTs, Pt/In_2O_3–TiO_2–NTs-(0, 9.4), and Pt/In_2O_3–TiO_2–NTs-(0.8, 9.4) materials.

The nitrogen adsorption-desorption isotherms of the TiO_2-based samples were presented in Fig.4a. The adsorption-desorption isotherms of TiO_2-based nanotubes indicated the type IV with H3 hysteresis loops, which according to BDDT classification was characteristic of a mesoporous material having pore sizes between 2 and 50 nm[24]. This was confirmed by the pore size distribution (Fig. 4b). Moreover, the formation of such mesoporous materials was attributed to the aggregation of the primary nanocrystallites. In the case of Pt/In_2O_3–TiO_2–NPs, its adsorption isotherm showed a Type IV with H2 hysteresis loop, which resulted from the synthesis methods difference. The textural parameters including BET surface

areas, pore volumes, and median pore diameters derived from N_2-adsorption measurements are summarized in Table 1 (ESI). From the above results it is found that doping In_2O_3 or In_2O_3 and Pt with TiO_2-based nanotubes resulted in decreases of BET surface areas (250.8 $m^2 g^{-1}$ – 65.1 $m^2 g^{-1}$) and that higher In_2O_3 or Pt loadings led to the smaller BET surface areas. As for the Pt/In_2O_3–TiO_2–NPs (134.8 $m^2 g^{-1}$), its BET surface area was slightly larger than that of the corresponding Pt/In_2O_3–TiO_2–NTs (123.7 $m^2 g^{-1}$), which resulted from the synthesis methods difference. In addition, with increasing in the calcination temperature from 573 K to 773 K, the BET surface area of the Pt/In_2O_3–TiO_2–NTs-(0.8, 9.4) gradually decreased from 237.6 $m^2 g^{-1}$ to 64.1 $m^2 g^{-1}$.

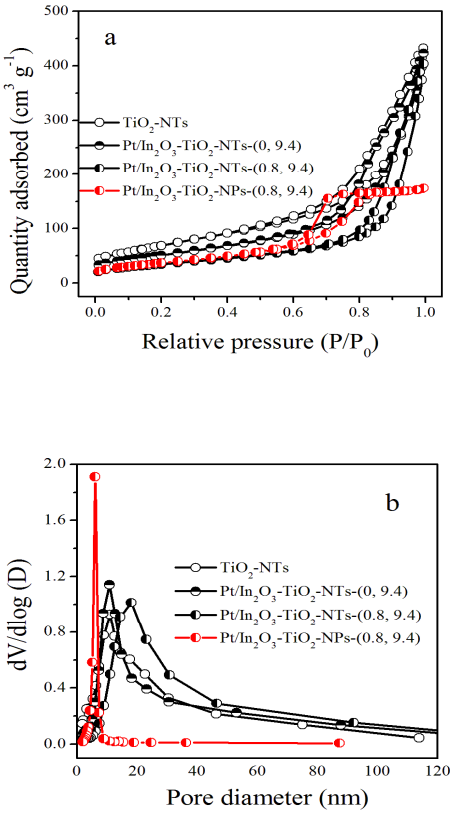

Fig. 4 Nitrogen adsorption/desorption isotherms (a) and pore size distribution profiles (b) of pure TiO_2–NTs, Pt/In_2O_3–TiO_2–NTs-(0, 9.4), Pt/In_2O_3–TiO_2–NTs-(0.8, 9.4), and Pt/In_2O_3–TiO_2–NPs-(0.8, 9.4) materials.

3.1.2. Morphology

FESEM and TEM were used to characterize the morphology and microstructures of the as-prepared nanotubes. As shown in Fig.5, the nanotubular morphology with an average diameter of 10 nm and length of 100 nm remained almost unchanged before and after In_2O_3 doping or In_2O_3 and Pt co-doping. Meanwhile, TiO_2–NTs and In_2O_3–TiO_2–NTs had clean and smooth surface (Fig. 5a-d). Compared the images of In_2O_3–TiO_2–NTs with Pt/In_2O_3–TiO_2–NTs, homogeneously dispersed metallic Pt particles with average size of

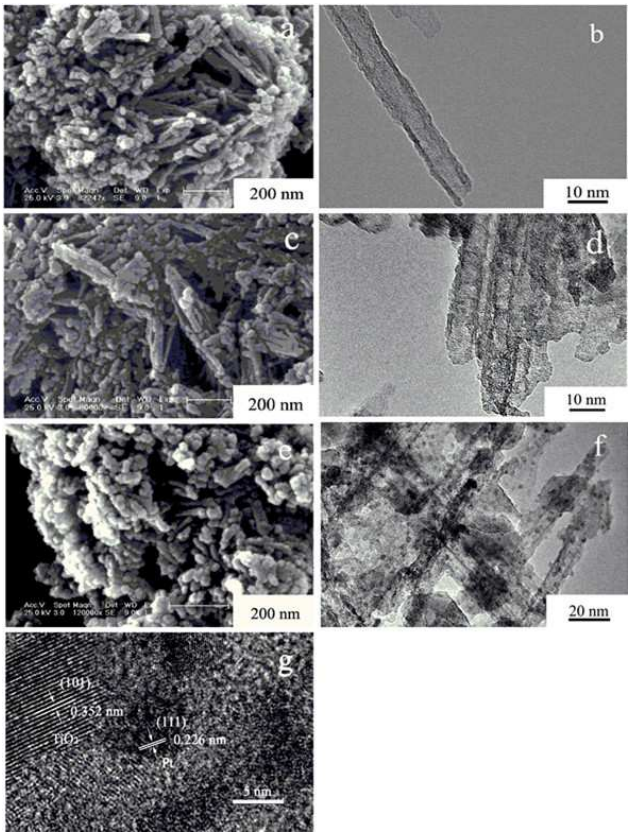

Fig. 5 FESEM and TEM images of TiO_2–NTs (a and b), Pt/In_2O_3–TiO_2–NTs-(0, 9.4) (c and d), and Pt/In_2O_3–TiO_2–NTs-(0.8, 9.4) (e and f), respectively. HRTEM images of Pt/In_2O_3–TiO_2–NTs-(0.8, 9.4) (g).

5 nm on both the inner and outer surfaces of the nanotubes can be clearly observed in Fig. 5e and f. HRTEM was used to investigate the crystal structure of the Pt/In_2O_3–TiO_2–NTs. Fig. 5g displayed two types of clear lattice fringes: one set of the lattice fringe was 0.352 nm, corresponding to the (101) plane of anatase crystal of TiO_2; the other set of the fringes was 0.226 nm, corresponding to the (111) lattice spacing of the cubic phase of metallic Pt nanoparticles[25]. However, lattice fringes corresponding to In_2O_3 was not seen. In addition, the HRTEM images of different Pt loading were shown in Fig. S1 of the ESI. The particle size of Pt in Pt/In_2O_3–TiO_2–NTs-(0.4, 9.4) and Pt/In_2O_3–TiO_2–NTs-(6.9, 9.4) was about 3 nm and 8 nm, respectively.

The connecting mode of Pt, In_2O_3, and TiO_2 in the Pt/In_2O_3–TiO_2–NTs material can be inferred by the combination of ionic radius data of In^{3+} and Ti^{4+} and TEM observation. That is, the ionic radius of the doping In^{3+} ion (81 pm) is larger than that of the lattice Ti^{4+} ion (60.5 pm)[26]. Accordingly, it is difficult for the In^{3+} ions to enter into the lattice of TiO_2, but it is energetically favorable for In^{3+} to reside in the interstitial site of TiO_2 lattice[27]. We therefore tentatively infer that the In_2O_3 homogeneously disperse throughout TiO_2 framework in the Pt/In_2O_3–TiO_2–NTs material, and both In_2O_3 and TiO_2 construct the wall structure of the nanotubes together; simultaneously, Pt nanoparticles (average size of 5 nm) are well distributed on both the inner and outer surfaces of the nanotubes.

3.1.3. Optical property

The UV–vis/DRS spectra of the different samples were presented in Fig. 6. As shown in Fig. 6a, compared with pure TiO_2–NTs, the absorption band of In_2O_3 doping TiO_2–NTs had a slight red-shift; moreover, the redshift was more obvious for Pt/In_2O_3–TiO_2–NTs-(0, 12.0) in comparison to Pt/In_2O_3–TiO_2–NTs-(0, 9.4). The decreased band gap of In_2O_3–TiO_2–NTs with respect to TiO_2–NTs originates from the contribution of In5s5p orbital to the conduction band of TiO_2[6]. Fig. 6b presented the UV–vis/DRS spectra of the different Pt doped In_2O_3–TiO_2–NTs. It is found that the absorption edges of Pt/In_2O_3–TiO_2–NTs had a slight buleshift compared with In_2O_3–TiO_2–NTs, attributing to the quantum size effect of the nanosized Pt particles; moreover, the blueshift was more obvious with the increasing of the Pt loading from 0% to 6.9%. Additionally, the absorption of Pt/In_2O_3–TiO_2–NTs in the range of 400 nm–800 nm was assigned to the SPR band of metallic Pt[14].

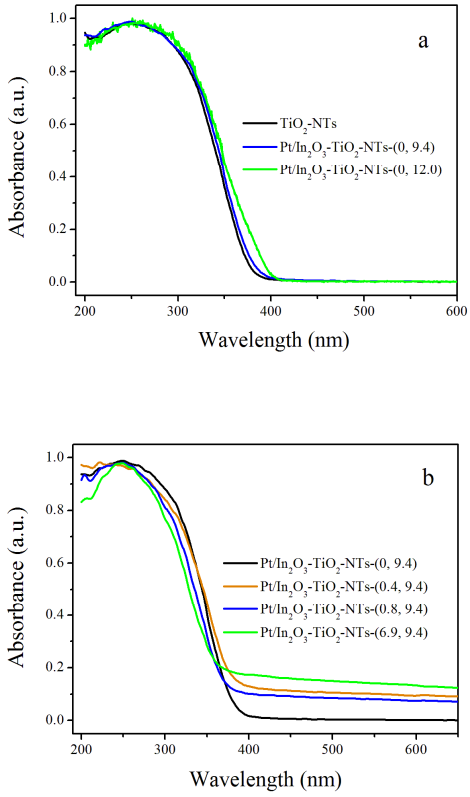

Fig. 6 UV-vis DRS of as-prepared (a) Pt/In_2O_3–TiO_2–NTs-(0, y) with y = 0, 9.4, and 12.0%, respectively; (b) Pt/In_2O_3–TiO_2–NTs-(x, 9.4) with x = 0, 0.4, 0.8, and 6.9%, respectively.

3.2. Photocatalytic test

3.2.1. Simulated sunlight photocatalytic degradation of RB

Adsorption capacity and simulated sunlight (320 nm < λ < 680 nm) photocatalytic activity of as-prepared Pt/In_2O_3–TiO_2–NTs materials were studied by degradation of an aqueous RB; meanwhile, the influences of In_2O_3 loadings, Pt loadings, and calcination temperature on the photocatalytic activity of Pt/In_2O_3–TiO_2–NTs were discussed.

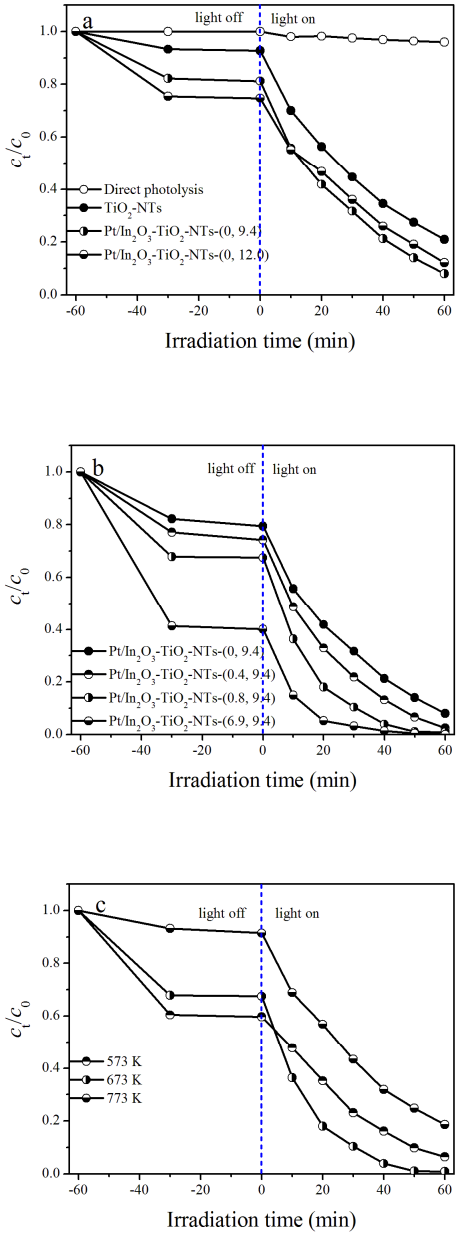

Fig. 7 Simulated sunlight (320 nm < λ < 680 nm) photocatalytic activity of Pt/In_2O_3–TiO_2–NTs materials towards RB degradation. (a) Influence of In_2O_3 loading, (b) Influence of Pt loading, and (c) Influence of the catalytic calcination temperatures. c_0 = 20 mg L^{-1}; volume: 100 mL; catalyst amount: 100 mg; light intensity: 0.3 W cm^{-2}.

Adsorption tests showed that: (i) it took 30 min to reach adsorption–desorption equilibrium; (ii) for the In_2O_3–TiO_2–NTs materials, they showed enhanced adsorption capacity to RB molecules with increasing In_2O_3 doping from 0 to 12.0% (Fig. 7a);

(iii) Pt/In_2O_3–TiO_2–NTs materials displayed higher adsorption capacity with increasing Pt loading (Fig. 7b). This was due to In_2O_3 or Pt doping increasing the negative charge on the titania surface, which promoted the adsorption of cationic dye RB[28]; and (iv) Pt/In_2O_3–TiO_2–NTs-(0.8, 9.4) material obtained at lower calcination temperature showed somewhat higher adsorption capacity compared with the materials obtained at higher calcination temperature (Fig. 7c), attributed to larger BET surface area of the former with respect to the latter (Table 1 in ESI).

Fig. 7a showed the influence of the In_2O_3 loading on the photocatalytic activity of the Pt/In_2O_3–TiO_2–NTs-(0, y). It indicates that the initial RB concentration was almost unchangeable under the solar simulating Xe lamp irradiation for 60 min. However, significant degradation of RB occurred in the presence of both the simulated sunlight irradiation and photocatalyst, it is found that the photocatalytic activity of the Pt/In_2O_3–TiO_2–NTs-(0, y) materials to RB degradation monotonically increased with the increase of In_2O_3 doping from 0% to 9.4%. Further increase In_2O_3 doping to 12.0% caused a slight decreased photocatalytic activity.

Fig.7b displayed the influence of the Pt loading on the photocatalytic activity of the Pt/In_2O_3–TiO_2–NTs-(x, 9.4). It is found that the photocatalytic activity of the Pt/In_2O_3–TiO_2–NTs materials to RB degradation monotonically increased with the increase of Pt doping from 0% to 6.9%. After 30 min simulated sunlight irradiation degradation of RB reached to 68.4% (Pt/In_2O_3–TiO_2–NTs-(0, 9.4)), 78.2% (Pt/In_2O_3–TiO_2–NTs-(0.4, 9.4)), 89.6% (Pt/In_2O_3–TiO_2–NTs-(0.8, 9.4)), and 96.8% (Pt/In_2O_3–TiO_2–NTs-(6.9, 9.4)), respectively. Therefore, Pt/In_2O_3–TiO_2–NTs-(6.9, 9.4) showed the highest photocatalytic activity among all tested photocatalysts.

Finally, the influence of the catalyst calcination temperature on the photoactivity of Pt/In_2O_3–TiO_2–NTs-(0.8, 9.4) was investigated in Fig. 7c. It can be observed that the simulated sunlight photocatalytic activity was enhanced as the annealing temperature increased from 573 to 673 K. Further increasing the temperature to 773 K led to the decreased activity.

3.2.2. Simulated sunlight photocatalytic degradation of DEP

To exclude dye sensitization, the adsorption and photocatalytic activity of as-prepared TiO_2-based materials were further evaluated by photodegradation of DEP that has no absorption in the visible area under simulated sunlight illumination (Fig. 8).

Adsorption tests showed that: (i) it took 30 min to reach adsorption–desorption equilibrium between DEP molecules and the catalyst; (ii) for the TiO_2-based materials with nanotube geometry, the adsorption capacity increased after the introduction of In_2O_3 and/or Pt regardless of their BET surface areas; (iii) compared with Pt/In_2O_3–TiO_2–NPs, Pt/In_2O_3–TiO_2–NTs showed stronger adsorption capacity, although both of them possessed similar BET surface area and the same Pt (0.8%) and In_2O_3 (9.4%) loading. The result implied the adsorption ability of the Pt/In_2O_3–TiO_2 materials was related to their morphology characteristics. The adsorption of DEP molecules on the Pt/In_2O_3–TiO_2 surface was due to the hydrogen bonding between the surface hydroxyl groups of TiO_2 (≡Ti–OH) and two carbonyl oxygen atoms of DEP molecules. Therefore, the number of surface ≡Ti–OH groups determined the adsorption ability of the Pt/In_2O_3–TiO_2 materials. Compared with Pt/In_2O_3–TiO_2–NPs, the open morphology of Pt/In_2O_3–TiO_2–NTs can provide more surface ≡Ti–OH groups to adsorb the DEP molecules, originating from the contribution of both the outer and inner surface of the materials. The conclusion is supported by FT-IR measurement (Fig. S2), showing that the peak intensities of ≡Ti–OH groups (situated at 3440 cm^{-1} and 1637 cm^{-1}) in the Pt/In_2O_3–TiO_2–NTs are somewhat higher. Similar explanation was reported by Lim's work[29].

Fig. 8 also indicated that the decrease of DEP concentration was negligible after the simulated sunlight irradiation for 45 min in the absence of photocatalyst. As for the TiO_2-based materials, their simulated sunlight photocatalytic activity followed the order Pt/In_2O_3–TiO_2–NTs-(0.8, 9.4) > Pt/In_2O_3–TiO_2–NTs-(0, 9.4) > Pt/In_2O_3–TiO_2–NPs-(0.8, 9.4) > TiO_2–NTs. The above results were consistent with those obtained for RB degradation.

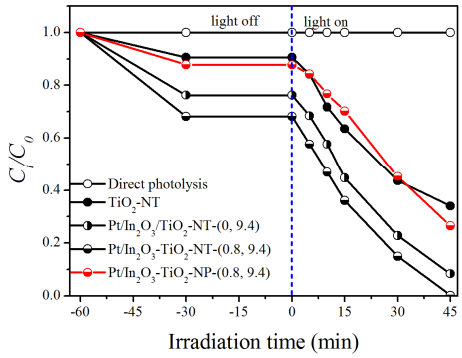

Fig. 8 Simulated sunlight (320 nm < λ < 680 nm) photocatalytic activity of TiO_2–NTs, Pt/In_2O_3–TiO_2–NTs, and Pt/In_2O_3–TiO_2–NPs materials towards DEP degradation. c_0 = 10 mg L^{-1}; volume: 100 mL; catalyst amount: 100 mg; light intensity: 0.3 W cm^{-2}.

To clarify the final products after decomposition, we measured the total organic carbon (TOC) in the residual solution after the photodegradation of DEP. Fig. S3 shows that the changes of TOC, which indicates that many DEP molecules were destroyed to form CO_2, H_2O, and other small molecules. However, the TOC conversion rations are not consistent with the photodegradation ration of DEP, which indicated that a part of DEP molecules only transferred to intermediate products. After 4 h simulated sunlight irradiation, the DEP mineralization reached to 86.3% with the Pt/In_2O_3–TiO_2–NTs-(0.8, 9.4) photocatalyst.

3.3. Recyclability of the catalyst

It should be noted that, for a photocatalyst to be commercially viable, stability and high activity of the photocatalyst are both indispensable. Herein, Pt/In_2O_3–TiO_2–NTs-(0.8, 9.4) was chosen to evaluate the recyclability of the catalyst. After the first catalytic run, the catalyst was removed by centrifugation and filtration, and then it was washed by hot water and ethanol for several hours, respectively. Subsequently, the catalyst was dried at 353 K for 24 h. The recovered catalyst was used for subsequent catalytic runs under the same experimental conditions. As shown in Fig. 9, no noticeable decrease of activity was observed for this photocatalyst by five times' DEP degradation reaction under simulated sunlight irradiation. The result was in accordance with the TEM and HRTEM

images. As displayed in Fig. S4, the Pt/In_2O_3–TiO_2–NTs-(0.8, 9.4) still maintained tubular morphology and the Pt particle size became a little bigger after recycling for five times. Thus, the Pt/In_2O_3–TiO_2–NTs-(0.8, 9.4) composite photocatalyst held an extraordinarily high stability and recyclability for photocatalytic applications.

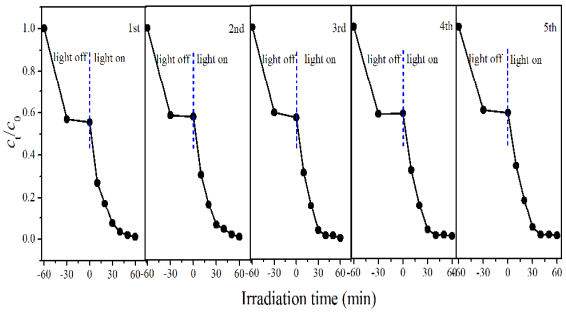

Fig. 9 Recyclability of Pt/In_2O_3–TiO_2–NTs-(0.8, 9.4) material for photocatalytic degradation of an aqueous RB under the simulated sunlight (320 nm < λ < 680 nm) irradiation. c_0 = 20 mg L^{-1}; volume: 100 mL; catalyst amount: 100 mg; light intensity: 0.3 W cm^{-2}.

3.4. Discussion

The above photocatalytic tests indicated that (1) for the TiO_2-based materials with nanotube geometry, the simulated photocatalytic activity of pure TiO_2–NTs could be further increased by introduction proper In_2O_3 and/or Pt loading; (2) Pt/In_2O_3–TiO_2–NTs-(0.8, 9.4) calcined at 673 K showed the highest photocatalytic activity under the different calcination temperature; (3) Pt/In_2O_3–TiO_2–NTs-(0.8, 9.4) showed manifestly higher activity than Pt/In_2O_3–TiO_2–NPs-(0.8. 9.4). The excellent photocatalytic activity of the Pt/In_2O_3–TiO_2–NTs was explained by the following crucial factors.

Firstly, both In_2O_3 and Pt co-doped TiO_2 nanotubes play the beneficial roles in improving the photocatalytic activity of TiO_2 by efficient separation of e_{CB}^-–h_{VB}^+ pairs. On the one hand, the conduction band (CB) bottom and the valence band (VB) top of TiO_2 lie at −0.4 and 2.8 eV (NHE), while the CB bottom and VB top of In_2O_3 lie at −0.63 and 2.17 eV (NHE), respectively [30]. Meanwhile, the band gap of In_2O_3 (2.8 eV) is lower than that of TiO_2 (3.2 eV). As a consequence, when In_2O_3 couple with TiO_2, the In_2O_3 can be excited under simulated sunlight irradiation and generates electrons in the In_2O_3, and then transfer to the conduction band (CB) of TiO_2, which leads to efficient separation of e_{CB}^-–h_{VB}^+ pairs. On the other hand, highly dispersed Pt nanoparticles on the inner and outer surfaces of In_2O_3–TiO_2 nanotubes can generate a Schottky barrier at the interface between Pt and TiO_2, which can capture effectively e_{CB}^- and promote the overall charge separation efficiency[31]. The band-gap structure of Pt/In_2O_3–TiO_2–NTs was proposed (Scheme 1). To further confirm the above explanation, the transient photocurrent responses of TiO_2-based nanotubes were measured under the UV-light irradiation. Fig. 10 depicted a comparison of photocurrent responses of different samples. It can be seen that Pt/In_2O_3–TiO_2–NTs/Ti and TiO_2–NTs/Ti electrode exhibited the highest and lowest photocurrent response, respectively. As for the Pt/In_2O_3–TiO_2–NTs/Ti electrode, high photocurrent meant more photoinduced electrons were transferred effectively from work electrode to counter electrode via external circuit, indicating high efficiency of electron-hole pair separation and transfer by introduction In_2O_3 and Pt in TiO_2 nanotubes.

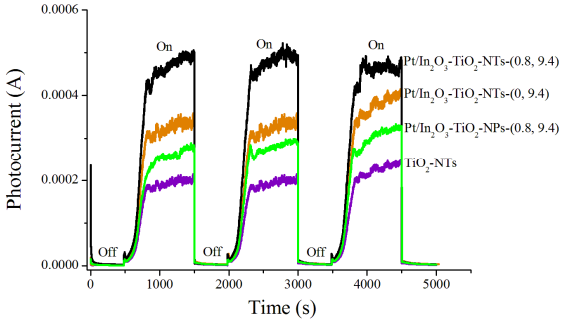

Fig. 10 Photocurrent responses of TiO_2-based Ti electrodes under UV light irradiation. 0.01 mol L^{-1} Na_2SO_4; the working electrode potential +1.0 V.

Secondly, in comparison to nanoparticles, open mesoporous morphology of nanotubes could facilitate the transport of the substance to the active sites during the photocatalytic reaction (Scheme 1)[3]; meanwhile, the unique structure makes better use of light through multiple reflections within its hollow space; beyond that, the nanotubes not only provided an efficient transport channel for photogenerated electrons but also improved the dispersion of Pt and In_2O_3 nanoparticles throughout the nanotubes, which in turn supressed the formation of the h_{VB}^+–e_{CB}^- recombination centers. This conclusion also can be evidenced by the photoelectrochemical experiment, showing that the photocurrent response of Pt/In_2O_3–TiO_2–NPs/Ti electrode is lower than Pt/In_2O_3–TiO_2–NTs/Ti electrode.

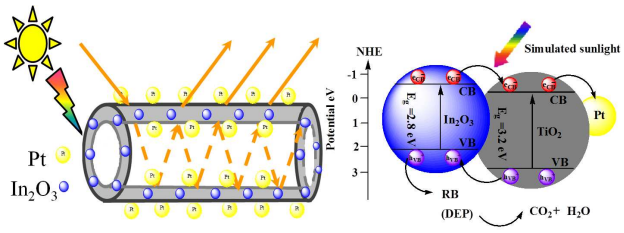

Scheme 1 Band gap structure and the simulated sunlight photocatalytic degradation of an aqueous RB (DEP) over the Pt/In_2O_3–TiO_2–NTs.

Finally, the crystallinity of the Pt/In_2O_3–TiO_2–NTs-(0.8. 9.4) material may be increased somewhat with increase the calcinations temperature from 573 K to 673 K, the well crystallized anatase could facilitate the transfer of the photoinduced electrons from bulk to surface, which promoted efficient separation of e_{CB}^-–h_{VB}^+ pairs. When the calcination temperature increased to 773 K, the crystallinity of the sample was further enhanced. However, BET area decreases from 123.7 m^2 g^{-1} to 64.1 m^2 g^{-1}. Meanwhile, the tubular structure began to collapse, subsequently lowered the

dispersion of Pt and In_2O_3 throughout TiO_2 nanotubes, and further increased the nanoparticles aggregation. These factors led to the decreased photocatalytic activity of Pt/In_2O_3–TiO_2–NTs-(0.8. 9.4) with increase the catalyst calcination temperature.

Conclusions

Pt/In_2O_3–TiO_2–NTs were fabricated via multicomponent assembly combined with solvothermal treatment. The prepared Pt/In_2O_3−TiO_2–NTs system exhibited considerably high simulated sunlight photocatalytic activity towards the degradation of RB and DEP, and its catalytic activity outperformed TiO_2–NTs, In_2O_3−TiO_2–NTs, and Pt/In_2O_3−TiO_2–NPs. This enhanced photocatalytic activity is due to more efficient separation of the h_{VB}^+–e_{CB}^- pairs, originating from the introduction of In_2O_3 and Pt within TiO_2 framework, the nanotubular geometries, and the crystallinity of the materials. It is believed that this result is of great importance in developing new photocatalysts for pollutant degradation.

Acknowledgements

This work was supported by the Natural Science Fund Council of China (21173036; 51278092; 51478095), and the Program for Young Teachers Scientific Research in Qiqihar University (2014K-M03). The work is also supported by the Program for New Century Excellent Talents in University of the Ministry of Education of China (NCET-13-0723).

Notes and references

1. Q.X. Deng, M.D. Wei, X.K. Ding, L.L. Jiang, B.H. Ye, K.M. Wei, *Chem. Commun.*, 2008, **31**, 3657–3659.
2. X.D. Wang, Z.D. Li, J. Shi, Y.H. Yu, *Chem. Rev.*, 2014, **114**, 9346−9384.
3. T. Wang, S. Wang, W.X. Chen, W. Wang, Z.L. Xu, Y. Liu, T. Horib, *J. Mater. Chem.*, 2009, **19**, 4692–4694.
4. G.L. Li, J.Y. Liu, G.B. Jiang, *Chem. Commun.,* 2011, **47**, 7443–7445.
5. H.X. Guo, J.H. Chen, W. Weng, Z.S. Zheng, D.F Wang，*J. Ind. Eng. Chem.*, 2014, **20**, 3081–3088.
6. X. Yang, Y.H. Wang, L.L. Xu, X.D. Yu, Y.H. Guo, *J. Phys. Chem. C*, 2008, **112** 11481–11489.
7. D. Shchukin, S. Poznyak, A. Kulak, P. Pichat, *J. Photochem. Photobiol., A*, 2004, **162**, 423–430.
8. B.K. Vijayan, N.M. Dimitrijevic, J.S. Wu, K.A. Gray, *J. Phys. Chem. C*, 2010, **114**, 21262–21269.
9. N. Liu, X.Y. Chen, J.L. Zhang, J.W. Schwank, *Catal. Today*, 2014, **225**, 34–51.
10. N. Pugazhenthiran, S. Murugesan, S. Anandan, *J. Hazard. Mater.*, 2013, **263**, 541– 549.
11. D.A. Wang, B.Yu, C.W. Wang, F. Zhou, W.M. Liu, *Adv. Mater.*, 2009, **21**, 1964–1967.
12. E. Ortel, S. Sokolov, R. Kraehnert, *Microporous Mesoporous Mater.*, 2010, **127**, 17–24.
13. M. Qamar, S.J. Kim, A.K. Ganguli, *Nanotechnology*, 2009, **20**, 455703–455710.
14. A.C. Chen, P. Holt-Hindle, *Chem. Rev.*, 2010, **110**, 3767–3804.
15. X.J. Feng, J.D. Sloppy, T.J. LaTempa, M. Paulose, S. Komarneni, N.Z. Bao, C.A. Grimes, *J. Mater. Chem.*, 2011, **21**, 13429–13433.
16. X.Y. Pan, Y.J. Xu, *J. Phys. Chem. C*, 2013, **117**, 17996−18005.
17. B. Abida, L. Chirchi, S. Baranton, T.W. Napporn, H. Kochkar, J.M. Léger, A. Ghorbel, *Appl. Catal. B: Environ.*, 2011, **106**, 609–615.
18. A.A. Ismail, D.W. Bahnemann, *Green Chem.*, 2011, **13**, 428–435.
19. H.Y. Chen, Z.B. Rui, H.B. Ji, *Ind. Eng. Chem. Res.*, 2014, **53**, 7629−7636.
20. J.C. Colmenares, A. Magdziarz, M.A. Aramendia, A. Marinas, J.M. Marinas, F.J. Urbano, J.A. Navio, *Catal. Commun.*, 2011, **16**, 1−6.
21. J.G. Yu, T.T. Ma, S.W. Liu, *Phys. Chem. Chem. Phys.*, 2011, **13**, 3491–3501.
22. L. Torrente-Murciano, A.A. Lapkin, D. Chadwick, *J. Mater. Chem.*, 2010, **20**, 6484–6489.
23. C. Ratanatawanate, C.R. Xiong, K.J. Balkus, Jr., *ACS Nano*, 2008, **2**, 1682–1688.
24. B.J. Vijayan, N.M. Dimitrijevic, T. Rajh, K. Gray, *J. Phys. Chem. C*, 2010, **114**, 12994–13002.
25. C.X. Wang, L.W. Yin, L.Y. Zhang, N.N. Liu, N. Lun, Y.X. Qi, *ACS Appl. Mater. Interfaces*, 2010, **2**, 3373–3377.
26. L. Xu, H.W. Song, B. Dong, Y. Wang, J.S. Chen, X. Bai, *Inorg. Chem.* 2010, **49**, 10590–10597.
27. R. Sasikala, A.R. Shirole, V. Sudarsan, Jagannath, C. Sudakar, R. Naik, R. Rao, S.R. Bharadwaj, *Appl. Catal. A-Gen.*, 2010, **377**, 47–54.
28. H. Tahiri, Y.A. Ichou, J.M. Herrmann, *J. Photochem. Photobiol., A*, 1998, **114**, 219–226.
29. Y.W. Lim, Y.X. Tang, Y.H. Cheng, Z. Chen, *Nanoscale*, 2010, **2**, 2751–2757.
30. J.B. Mu, B. Chen, M.Y. Zhang, Z.C. Guo, P. Zhang, Z.Y. Zhang, Y.Y. Sun, C.L. Shao, Y.C. Liu, *ACS Appl. Mater. Interfaces*, 2012, **4**, 424−430.
31. H.Q. An, J. Zhou, J.X. Li, B.L. Zhu, S.R. Wang, S.M. Zhang, S.H. Wu, W.P. Huang, *Catal. Commun.*, 2009, **11**, 175−179.

Graphical abstract

Title: Fabrication and enhanced the simulated sunlight photocatalytic activity of metallic platinum and indium oxide codoped titania nanotubes

Authors: Fengyan Ma,[a,]* Zhi Geng[b] and Jiyan Leng[c]

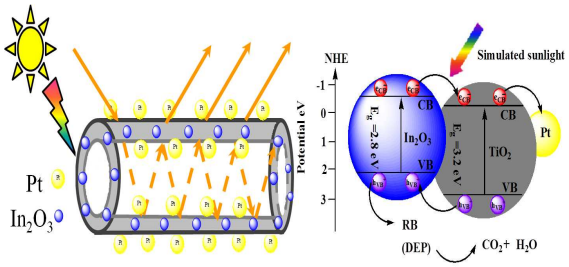

$Pt/In_2O_3–TiO_2–NTs$ were fabricated by multicomponent assembly-solvothermal treatment, and showed excellent activity originated from improved quantum yield and nanotubular geometries.